Available online at www.sciencedirect.com

SciVerse ScienceDirect

Ceramics International 39 (2013) 6559–6568

CERAMICS INTERNATIONAL

www.elsevier.com/locate/ceramint

Study of electrochemical hydrogen charge/discharge properties of $FePO_4$ for application as negative electrodes in hydrogen batteries

Dae-Kwang Lim[a], Bhupendra Singh[a,b], Jungwon Kang[c], Jaekook Kim[c], Sun-Ju Song[a,b,*]

[a]*Ionics Lab, School of Materials Science and Engineering, Chonnam National University, 300 Yongbong-dong, Buk-gu, Gwang-Ju 500-757, Republic of Korea*

[b]*Research Institute for Catalysis, Chonnam National University, Gwang-Ju 500-757, Republic of Korea*

[c]*Laboratory for Energy Materials Synthesis, School of Materials Science and Engineering, Chonnam National University, 300 Yongbong-dong, Buk-gu, Gwang-Ju 500-757, Republic of Korea*

Received 14 December 2012; received in revised form 25 January 2013; accepted 27 January 2013
Available online 1 February 2013

Abstract

We report the electrochemical hydrogen charge/discharge properties of electrodes containing crystalline and amorphous $FePO_4$ as active material in KOH electrolyte. Crystalline and amorphous $FePO_4$ were synthesized by an alcohol-assisted precipitation method, and the powders obtained were characterized by X-ray diffraction. X-ray photoelectron spectroscopy is used to investigate the mechanism of hydrogen charge/discharge behavior of $FePO_4$. The electrochemical hydrogen charge/discharge properties of electrodes containing crystalline and amorphous $FePO_4$ were investigated for potential application as negative electrodes in rechargeable hydrogen batteries. In galvanostatic discharge/charge mode at 25 °C, the crystalline $FePO_4$ showed a maximum discharge capacity of 109 mA h g^{-1}, while the amorphous $FePO_4$ showed a maximum discharge capacity of 81.4 mA h g^{-1}. The electrochemical kinetic properties, exchange current density, and proton diffusivity were calculated using linear polarization measurement and the potential-step method.

Keywords: Iron(III) phosphate; Electrochemical hydrogen charge/discharge; Negative electrode; Hydrogen batteries

1. Introduction

Increasing concern about environmental pollution and the rapid exhaustion of conventional fossil fuels has made electricity-powered vehicles a preferable future mode of transportation and, therefore, the development of efficient, durable, economically affordable, and environmentally friendly energy conversion and storage devices has become a key issue for the transition from petroleum-powered vehicles to electricity-powered vehicles [1]. Among various battery systems used in electric vehicles, Li-ion and nickel/metal-hydride (Ni–MH) batteries are considered to be more suitable because of their high energy density and better environmental compatibility [2]. However, due to some concerns related to safety issues and higher material-costs of Li-ion batteries, the Ni–MH batteries are being considered as preferable options in portable power applications [3]. The major advantages of using Ni–MH batteries are high power density, module flexibility, safe operation at high voltage and high temperature, high tolerance to over-charge and over-discharge, the use of environmentally compatible and recyclable materials, and low operational and maintenance costs [4].

The performance of Ni–MH batteries strongly depends on the intrinsic properties of the active materials used in its negative electrode [3]. Many traditional hydrogen storage alloys have been employed as negative electrodes in Ni–MH batteries, which include rare-earth-based AB_5-type alloys [5,6], AB_2-type alloys [7], AB-type alloys [8], and Mg-based alloys [9,10]. However, none of these are currently favored for widespread application because of their drawbacks, e.g. the capacities of AB_5-type alloys are ~300 mA h g^{-1} which

*Corresponding author at: Ionics Laboratory, School of Materials Science and Engineering, Chonnam National University, 300 Yongbong-dong, Buk-gu, Gwang-Ju 500-757, Republic of Korea. Tel.: +1 82 62 530 1706; fax: +1 82 62 530 1699.

E-mail addresses: song@chonnam.ac.kr, song@jnu.ac.kr (S.-J. Song).

0272-8842/$ - see front matter © 2013 Elsevier Ltd and Techna Group S.r.l. All rights reserved.
http://dx.doi.org/10.1016/j.ceramint.2013.01.089

is insufficient for portable electric devices and vehicles, AB_2-type alloys suffer from slow activation and low rate capabilities [11,12], and Mg-based alloys suffer from poor hydriding/dehydriding kinetics at room temperature and rapid degradation in alkaline solution due to the formation of $Mg(OH)_2$ passive films [13]. In the last decade, rare-earth-Mg–Ni-based alloys, which exhibited high discharge capacity and fast electrochemical kinetics, have become most promising anode materials for high energy and high power Ni–MH batteries [14–16]. In order to develop Ni–MH batteries with high performance and lower cost, a few potential hydrogen storage materials, such as Ti–V-based multicomponent multiphase alloys [17,18] and proton conducting perovskite-type oxides [19–21], have been reported recently.

The purpose of the present study is to explore the possibility of using Iron(III) phosphate ($FePO_4$) as a negative electrode material for hydrogen batteries. $FePO_4$ is an inexpensive, nontoxic, and environmentally benign material that has generally been used in practical applications such as heterogeneous catalysis [22], corrosion inhibition [23], and cathodes and anodes for lithium ion batteries [24–27]. In order to improve the electrochemical performance of $FePO_4$ in Li batteries, various researchers have employed strategies of modifications of the $FePO_4$ structure, such as crystalline or amorphous, hydrate or anhydrous [28–33]. In the present study, we have synthesized amorphous and crystalline $FePO_4$, and analyzed their electrochemical hydrogenation/dehydrogenation capacity for the application as negative electrode material for hydrogen batteries.

2. Materials and methods

2.1. Sample preparation

Amorphous and crystalline $FePO_4$ was synthesized by an alcohol-assisted precipitation method [34]. Briefly, iron acetate [$Fe(CH_3COO)_3$, 99.995%, Aldrich] and phosphoric acid [H_3PO_4, $\geq 85\%$, Dae Jung], in 1:1 stoichiometric ratio, were separately dissolved in distilled water. Methanol was added to the $Fe(CH_3COO)_3$ solution to form soluble $Fe(OH)_x(CH_3O)_{3-x}$-type complex. Phosphoric acid solution was slowly added to the $Fe(OH)_x(CH_3O)_{3-x}$ complex solution, and the resulting mixture was kept under stirring for 4 h which led to the precipitation of $FePO_4 \cdot nH_2O$ agglomerates. The resulting precipitate was filtered and repeatedly washed with methanol and acetone to remove organic impurities. The hydrated sample was vacuum dried at 250 °C for 12 h, which led to the formation of amorphous $FePO_4$. A part of the amorphous $FePO_4$ powder was annealed in argon atmosphere at 700 °C for 12 h to obtain crystalline $FePO_4$.

2.2. Structural characterization

The phase structure and the purity of $FePO_4$ powders were examined by powder X-ray diffraction (XRD). XRD data of the $FePO_4$ powder samples were collected using an X-ray diffractometer (XRD-7000, Shimadzu) equipped with a CuK_α radiation source (1.5406 Å), operating at 40 kV and 30 mA at a scan rate of 1°/min between the scanning angles (2θ) of 10° and 80°. The primary grain size (d) in the crystalline $FePO_4$ was obtained from the X-ray line width using the Scherrer formula, $d=0.9\lambda/(\beta_{1/2}\cos\theta)$, where λ is the X-ray wavelength, $\beta_{1/2}$ the corrected width of the main diffraction peak at half-height, and θ the diffraction angle. The microstructure of various $FePO_4$ samples was analyzed by scanning electron microscopy (Shimadzu, SS-550, Kyoto, Japan).

2.3. Electrochemical measurements

The hydrogen charge and discharge performance of each sample was estimated using a three-electrode electrochemical cell. In order to fabricate a working electrode, the prepared $FePO_4$ powder was mixed with carbon black, which acts as a current distributor, and planetary-milled in a zirconia pot at 200 rpm for 5 h. A slurry was made by adding 5% aqueous solution of polyvinyl alcohol (PVA) as a binder to the ball-milled mixture. The weight ratio of $FePO_4$, carbon black, and PVA in the slurry was 7.5:1.5:1 respectively. The resultant slurry was pasted onto a porous nickel gauze substrate (3 cm × 3 cm), and dried at ~70 °C for 5 h. The Ni-gauze substrate filled with electrode mixture paste was uniaxially pressed to a thickness of ~1 mm, and used as a working electrode in the electrochemical analysis. Electrochemical measurements were performed by a three-electrode cell consisting of a working electrode (containing $FePO_4$ sample), Pt counter electrode, and Hg/HgO reference electrode. In order to test the hydrogen storage ability of amorphous and crystalline $FePO_4$, the hydrogen charge/discharge performance was measured with 6 M KOH electrolyte solution at different temperatures (25–55 °C). The charge/discharge currents were determined by the sample weight and measured using a galvanostatic method (Wonatech, WBCS 3000). All working electrodes were charged at 20 mA g^{-1} for 5 h, then discharged to −0.3 V (vs. Hg/HgO) at the same current density.

An advanced electrochemical system (GAMRI Reference 3000) was used to evaluate the hydrogen proton diffusion coefficient (D) and the exchange current density (I_0) of $FePO_4$ using the potential-step and linear polarization methods, respectively. The electrodes were fully charged during the potentiostatic step discharge process, and then an overpotential of +500 mV was applied to them. An electrochemical analyzer was used to record the current–time transient curves after the potential step. In addition, the linear polarization curves of the electrodes were plotted by scanning the electrode potential at a rate of 0.1 mV s^{-1} from −5 to 5 mV (vs. open circuit potential) at 50% of the discharge depth.

X-ray photoelectron spectroscopy (XPS) analysis was performed using a VG Multilab 2000 spectrometer (Thermo

VG Scientific) in an ultra-high vacuum with an unmonochromatized MgK_{α} (1253.6 eV) X-ray source and a spherical section analyzer. Survey scan data and core peak data were collected using pass energies of 50 and 20 eV, respectively. The charge neutralization was not used in this experiment. In all cases, the spectra were charge referenced to hydrocarbon contamination C 1s peak at a binding energy of 284.5 eV.

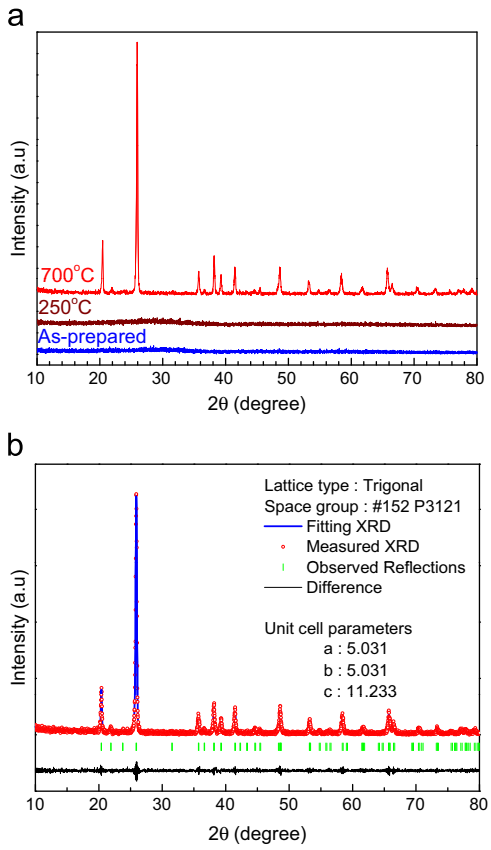

Fig. 1. (a) XRD patterns of $FePO_4$ as-prepared $FePO_4$, the $FePO_4$ sample vacuum-annealed at 250 °C, and $FePO_4$ sample annealed in argon at 700 °C, and (b) Rietveld fit to the X-ray diffraction data of the crystalline $FePO_4$ sample annealed in argon at 700 °C.

3. Results and discussion

3.1. Phase structure and microstructure characterization

Fig. 1(a) shows the XRD profiles of as-prepared $FePO_4$ sample, $FePO_4$ sample annealed in vacuum at 250 °C, and $FePO_4$ sample annealed in argon at 700 °C. The as-prepared sample and the sample vacuum annealed at 250 °C showed amorphous characteristics. The XRD pattern of the sample annealed at 700 °C in argon, however, showed a well-developed crystalline structure with peaks corresponding to a trigonal lattice. The Rietveld refinement of the XRD pattern of crystalline $FePO_4$ is shown in Fig. 1(b). No extra peaks were detected in any other planes, except those for the trigonal lattice, which indicates a high level of phase purity of the crystalline $FePO_4$ sample. The refined trigonal unit cell parameters for crystalline $FePO_4$ at ambient temperature were $a=5.031$ Å, $b=5.031$ Å, and $c=11.233$ Å. The primary grain size (d) in the crystalline $FePO_4$ obtained from the X-ray line width using Scherrer equation was 40.5 nm.

Fig. 2 shows the SEM image of $FePO_4$ powders. As the amorphous $FePO_4$ [Fig. 2(a)] was obtained by vacuum drying of the as-prepared sample at a mild temperature of 250 °C, it was weakly agglomerated, and the size of individual particles was ~20 nm. On the other hand, crystalline $FePO_4$ [Fig. 2(b)] was obtained by annealing amorphous $FePO_4$ powder in argon atmosphere at 700 °C, therefore, they are in the form of larger grains than those in the amorphous $FePO_4$, as annealing at higher temperature has resulted in grain growth.

3.2. Electrochemical hydrogen charge/discharge properties

Fig. 3 shows the charge–discharge curves of the amorphous and crystalline $FePO_4$ at different temperatures, where charge and discharge means the incorporation and dissolution of hydrogen–proton, respectively. The appearance of a long and flat potential plateau is possibly due to the formation of stable chemical bonds between hydrogen atoms and the oxygen of $FePO_4$ [35]. It is evident from the charge/discharge curves of

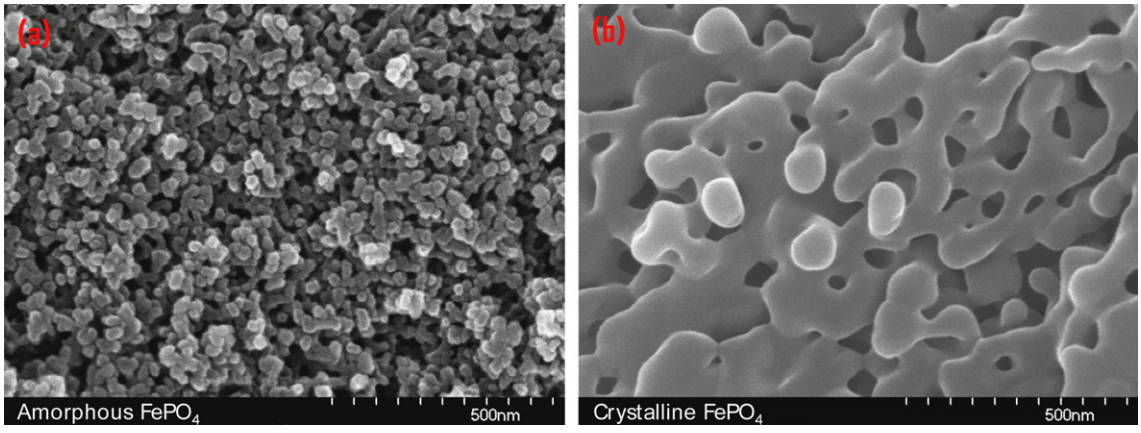

Fig. 2. SEM image of (a) amorphous $FePO_4$ and (b) crystalline $FePO_4$.

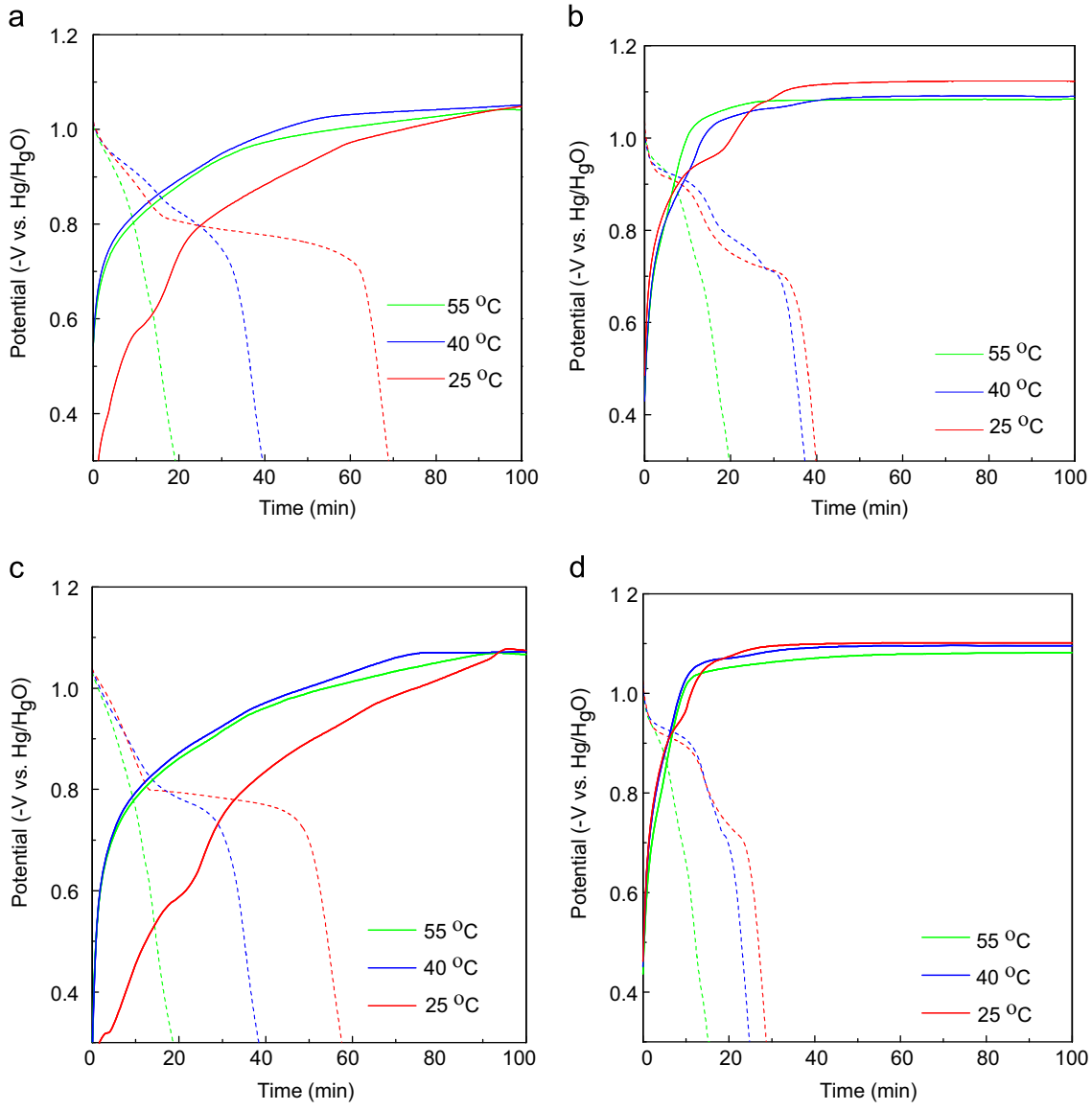

Fig. 3. Charge–discharge curves of amorphous $FePO_4$ electrode at the 1st cycle (a) and 20th cycle (b), and crystalline $FePO_4$ electrode at the 1st cycle (c) and 20th cycle (d) at different temperatures (solid lines represent charging and dashed lines represent discharging).

the 1st cycle [Fig. 3(a) and (c)] that at 25 °C, both amorphous and crystalline $FePO_4$ undergo slow charging/discharging, and take a long time to reach the plateau value of potential (~1.05 V) while charging. However, when the temperature was raised, the $FePO_4$ electrodes show fast charging/discharging, and the plateau value of potential is quickly reached. On the other hand, in 20th cycle [Fig. 3(b) and (d)], both the amorphous and crystalline $FePO_4$ undergo fast charge/discharge, and the plateau value of potential is quickly reached at all the temperatures measured. This indicates that the $FePO_4$ electrodes needed some initial activation during the charging/discharging process.

3.3. Mechanism of electrochemical hydrogen charge/discharge

XPS analysis was carried out in order to get information about the oxidation state of the transition metal species on charging. The deconvolution of XPS spectra was done using a non-linear least-square fitting algorithm and the results are shown in Fig. 4. The spectrum for the uncharged crystalline $FePO_4$ (Fig. 4a) showed the presence of two well-resolved spectral lines in the Fe 2p region at ~712 and 725 eV, respectively assigned to the binding energies of an electron in Fe $2p_{3/2}$ and Fe $2p_{1/2}$ spin–orbit components. The oxidation state of Fe in uncharged $FePO_4$ was almost exclusively Fe^{+3}. However, the oxidation state of Fe in the charged sample (Fig. 4b) was dominated by Fe^{+2}. This suggests that during the charging process Fe^{+3} is reduced to Fe^{+2} and hydrogen–proton is incorporated into the material to charge compensate the effective negative charge created due to the reduction of Fe^{+3} ion. Similarly, in the discharge process, the removal of hydrogen–proton from the $FePO_4$ electrode would change the oxidation state of Fe from +2 to +3 for the sake of charge compensation. The oxidation state of Fe in the discharged

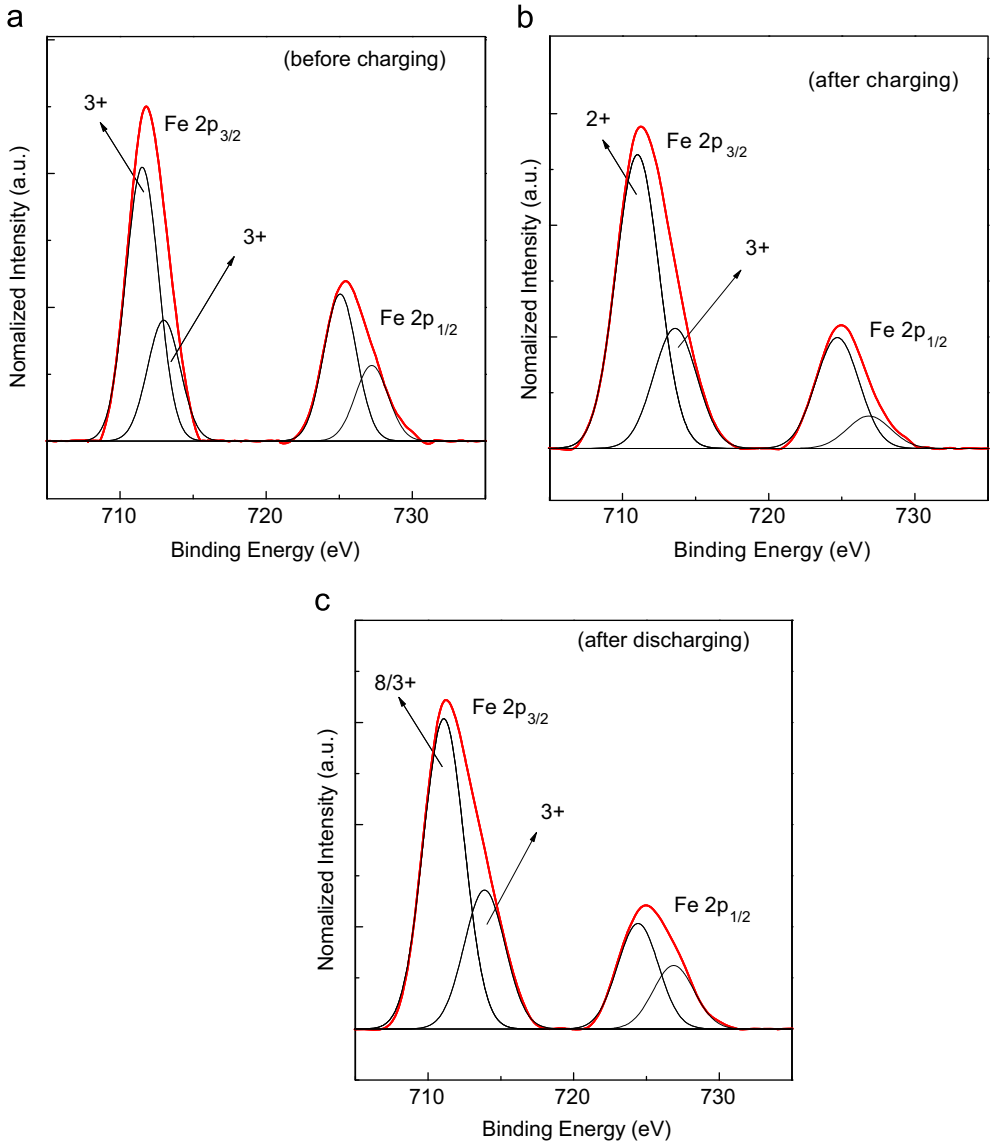

Fig. 4. XPS patterns of (a) uncharged, (b) charged, and (c) discharged crystalline $FePO_4$.

sample is not completely changed to +3 (Fig. 4c), which could be due to the formation of some irreversible products which could not be re-oxidized to Fe^{+3} state. However, based on the XPS data of crystalline $FePO_4$, the hydrogen storage properties of $FePO_4$ electrodes may be interpreted by a change in valance state of transition metal ion and the charge and discharge mechanism can be analogized as a reaction based on the redox cycle of Fe ions, as shown below in Eq. (1):

$$Fe^{3+}PO_4 + xH_2O + xe^- \underset{\text{Discharge}}{\overset{\text{Charge}}{\rightleftarrows}} H_x^+ Fe_x^{2+} Fe_{1-x}^{3+} PO_4 + xOH^- \quad (1)$$

3.4. Cycle-ability of $FePO_4$ during charge/discharge

The cyclic discharge properties of the $FePO_4$ electrodes at various temperatures and under a charge/discharge current density of 20 mA g^{-1} are shown in Fig. 5. At every measurement temperature, a slight increase in discharge capacity was observed for the first 2–4 cycles for all $FePO_4$ electrodes, suggesting a process of initial electrode activation. This behavior is similar to that observed in traditional hydrogen storage alloys, such as AB_2, AB_5 and La–Mg–Ni, in hydrogen batteries [36–38]. A gradual decrease in discharge capacity, however, was observed in the subsequent cycles. The initial hydrogen absorption reaction during charging leads to volume expansion of the $FePO_4$, resulting in an increase in the effective surface area of the electrode, similar to that observed for some metal hydride electrodes [39], and subsequent electrode activation. Although presently we could not figure out the exact reason, we suspect that the initial activation of $FePO_4$ is different from that in the case of traditional hydrogen storage alloys, where initial activation was observed due to the removal of passive oxide layer by initial cycling. However, the comparison of XPS spectra of uncharged

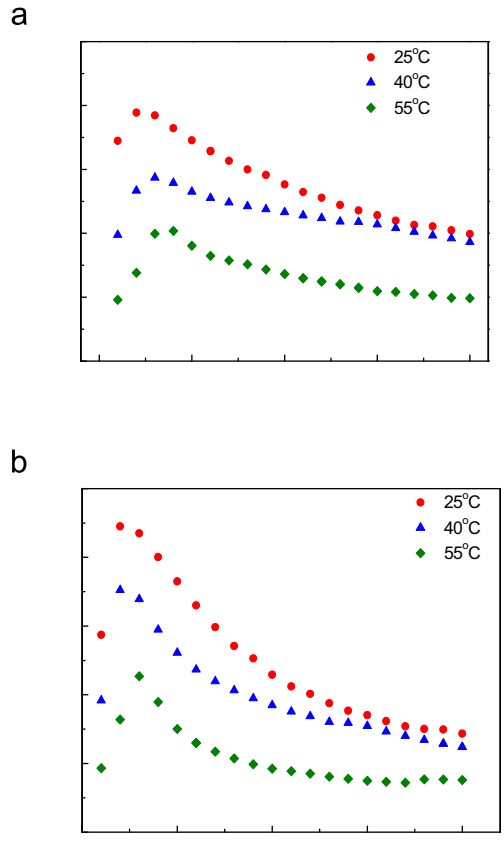

Fig. 5. Discharge capacity versus cycle number of (a) amorphous $FePO_4$ electrode and (b) crystalline $FePO_4$ electrode under the discharge current density of 20 mA g^{-1}.

$FePO_4$ (Fig. 4a) and charged $FePO_4$ (Fig. 4b) shows that there is a shift in the position of the XPS peaks after charging, which indicated that there is some structural rearrangements occurring during the initial charging and they can be responsible for the initial activation. The repeated hydrogen–proton absorption/desorption during cyclic charging/discharging, however, may cause fractures in the working electrode due to repeated volume expansion/contraction, leading to the pulverization and loss of active material from the working electrode, and therefore, a decrease in the cyclic capacity of $FePO_4$. However, we suspect that the loss of cyclic capacity of $FePO_4$ in the present measurement is more related to the overall stability of working electrode, as discussed subsequently in Section 3.6. It can also be seen that the discharge capacities decreased with an increase in temperature, which is similar to the traditional hydrogen storage alloys used in hydrogen batteries [40]. Although the cyclic stability data obtained in the present study might not appear very promising at first, we suspect this could be due to the method employed in the electrode fabrication using active material. We hope that the cycle-ability of the $FePO_4$ electrodes can be improved by just improving the stability of the active material on the working electrodes.

The theoretical capacity of $FePO_4$ for 1 electron transfer per $FePO_4$ is ~177 mA h g^{-1}. The value of maximum discharge capacity at 25 °C for crystalline $FePO_4$ was 89.0 mA h g^{-1} and that for amorphous $FePO_4$ was 77.8 mA h g^{-1}, indicating that the crystalline $FePO_4$ has higher initial discharge capacity than the amorphous $FePO_4$. Although the crystalline $FePO_4$ has higher initial discharge capacity, the decrease in cyclic discharge capacity is less sharp for amorphous $FePO_4$ than for crystalline $FePO_4$, and after 7–10 cycles, the amorphous $FePO_4$ shows higher discharge capacities than the crystalline $FePO_4$, as shown in Fig. 5, indicating that the amorphous $FePO_4$ is less prone to pulverization. It is possible that the random structure of the amorphous $FePO_4$ could more easily accommodate the repeated insertion/removal of hydrogen–protons during the charging/discharging process than the ordered structure of crystalline $FePO_4$.

Fig. 6 shows the variation of discharge capacity vs. different charge capacities during successive cycles at 25 °C at a discharge rate of 100 mA g^{-1}. During the first cycle, when the charge capacity was 100 mA h g^{-1}, the discharge capacity was 55 mA h g^{-1} for amorphous $FePO_4$ and 48 mA h g^{-1} for crystalline $FePO_4$. During the second cycle, when the charge capacity was increased to 200 mA h g^{-1}, the discharge capacities reached 71.3 mA h g^{-1} and 93 mA h g^{-1} for amorphous $FePO_4$ and crystalline $FePO_4$, respectively. However, during the subsequent 3rd–5th cycles, when the charge capacity was further raised from 300 to 500 mA h g^{-1}, the discharge capacities of both amorphous $FePO_4$ and crystalline $FePO_4$ did not change significantly, remaining around 80 mA h g^{-1} and 109 mA h g^{-1}, respectively. Comparing the results of Figs. 5 and 6, it appears that the initial charging at 20 mA g^{-1} for 5 h was not enough for both amorphous $FePO_4$ and crystalline $FePO_4$ electrodes. When the charging capacity was raised, the materials reached their real capacity to change Fe^{+3} to Fe^{2+} during the charging process. Therefore, the maximum discharge capacities of amorphous and crystalline $FePO_4$ should be considered as 80 and 109 mA h g^{-1}, respectively.

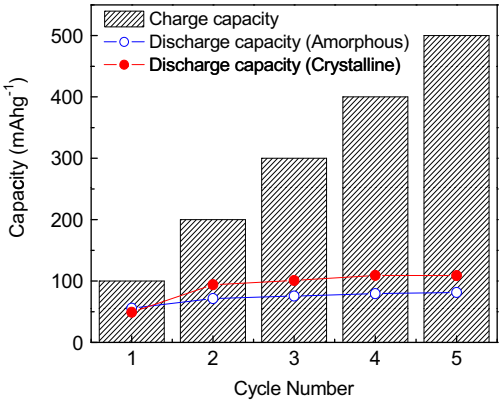

Fig. 6. Discharge capacity of amorphous and crystalline $FePO_4$ electrode as a function of cycle number for different charge capacities at 25 °C.

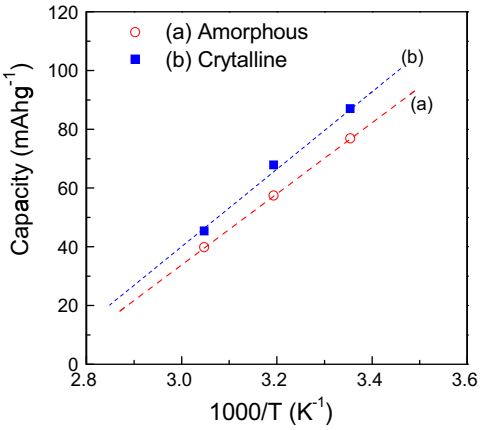

Fig. 7. Variation of discharge capacity (in 3rd cycle) vs. temperature of (a) amorphous $FePO_4$ electrode and (b) crystalline $FePO_4$ electrode.

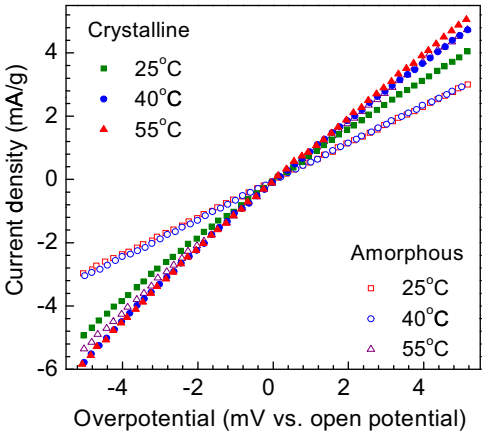

Fig. 8. Linear polarization curves of amorphous $FePO_4$ and crystalline $FePO_4$ electrodes.

Fig. 7 shows the variation of discharge capacity in the 3rd cycle for crystalline and amorphous $FePO_4$ with temperature. The plots show the Arrhenius behavior, and the slope of the lines indicates that the discharge is an exothermic process. It is evident from Fig. 7 that for both amorphous and crystalline $FePO_4$, the discharge capacity decreases with the increase in temperature.

3.5. Kinetic characteristics

The exchange current density (I_0), which is a measure of the forward and reverse electrode reaction rate at the equilibrium potential, can be used to characterize the electro-catalytic activity of the charge-transfer reaction on the electrode surface. The exchange current density may be calculated from the polarization resistance (R_p) using the simplified Butler–Volmer equation (2) at low overpotential limit conditions:

$$I_0 = \frac{RT}{FR_p} \tag{2}$$

where R is the gas constant (J/mol K), T is the absolute temperature (K), and F is the Faraday constant (C/mol). Fig. 8 shows the linear polarization curves of amorphous and crystalline $FePO_4$ electrodes. The values of polarization resistance R_p can be obtained from the linear polarization curves of the $FePO_4$ electrodes, and consequently, I_0 can be calculated. The calculated values of the exchange current densities were 15.03, 16.23, and 27.88 mA g^{-1} for amorphous $FePO_4$, and 22.26, 27.47, and 31.16 mA g^{-1} for crystalline $FePO_4$ at 25, 40, and 55 °C, respectively. From these values, it can be seen that for both the amorphous and crystalline $FePO_4$, the current densities increase with the increase in temperature, indicating that the rate of charge transfer at the electrodes increases with the increasing temperature. Also, the current densities obtained for crystalline $FePO_4$ are higher than those for amorphous $FePO_4$, indicating that the ordered structure of crystalline $FePO_4$ facilitates the charge transfer at the electrodes.

The hydrogen–proton diffusion rate was estimated using the potential-step method. Fig. 9 shows the typical time dependence of anodic current density during the discharge process of $FePO_4$ electrodes from their fully-charged states. As indicated by Fig. 9, after a logarithmic decay at the initial stage for a short time period, a linear relationship is observed for a long time period, which suggests that initially, there is rapid diffusion of hydrogen–proton from the surface, which is followed by the diffusion of hydrogen–proton in the bulk of $FePO_4$ electrodes. When the electrode reactions are controlled by the diffusion of hydrogen–proton in $FePO_4$ bulk, the hydrogen–proton diffusion coefficient (D) can be calculated by the following equation:

$$\log i = \log\left(\pm\frac{6FD}{da^2}(c_0 - c_s)\right) - \frac{\pi^2}{2.303}\frac{D}{a^2}t \tag{3}$$

where i is the anodic current density (mA g^{-1}), D the hydrogen diffusion coefficient ($cm^2\ s^{-1}$), d is the density of the $FePO_4$ electrode (g cm^{-3}), a is the mean radius of the $FePO_4$ particles (cm), c_0 is the initial hydrogen concentration in the bulk of the $FePO_4$ (mol cm^{-3}), c_s is the surface hydrogen concentration of the $FePO_4$ electrode (mol cm^{-3}), and t is the discharge time (s). The calculated values of D at 25, 40, and 55 °C for the amorphous $FePO_4$ were 3.85×10^{-16}, 1.68×10^{-16}, and 1.32×10^{-16} $cm^2\ s^{-1}$ respectively, and for crystalline $FePO_4$, they were 1.43×10^{-15}, $1.90 \times 10,^{-15}$ and 1.96×10^{-15} $cm^2\ s^{-1}$, respectively. In general, the values of D for crystalline $FePO_4$ are nearly one order higher than the values of D for amorphous $FePO_4$, indicating a facilitated diffusion of hydrogen–proton in the material bulk in crystalline $FePO_4$ compared to amorphous $FePO_4$. On the other hand, the values of D decreased with the increasing temperature from 25 °C to 55 °C for amorphous $FePO_4$, but for crystalline $FePO_4$, the value of D increased with the increasing temperature from 25 °C to 55 °C.

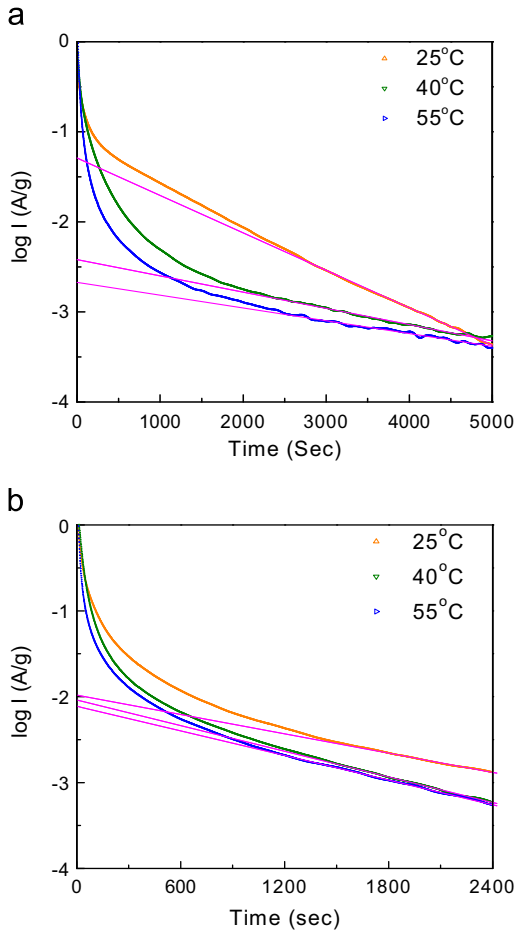

Fig. 9. Constant potential discharge curves of (a) amorphous $FePO_4$ electrodes and (b) crystalline $FePO_4$ electrodes at different temperatures.

3.6. Comment on stability of working electrode affecting charge/discharge capacity and cycle-ability during charge/discharge measurement

The cyclic stability data obtained in the present study might not appear very promising at first, and we suspect this could be due to the method employed in the fabrication of working electrode using the active material. As discussed earlier in Section 3.3, there was a decrease in discharge capacity of the material during long term cyclic operation. The formation of some non-rechargeable products, which is inevitable in aqueous electrolytes, could be the reason for this [41,42]. However, formation of such products could be suppressed by adding suitable additives to the $FePO_4$ to enhance the performance [41,42]. Apart from this, there are a number of other factors associated with the measurement setup which could also contribute to the loss of cyclic stability. During the half-cell measurement, for example, the cell was not completely sealed. Therefore, a part of KOH electrolyte may react with the atmospheric CO_2 and form K_2CO_3. This would lead to a decrease in actual concentration of the electrolyte with the passage of time and decrease in discharge current, thus affecting cyclic-ability of the material. Furthermore, for the half-cell used in charge/discharge measurement, the working electrode was fabricated using carbon black (as a current distributor) and PVA as a binder. Being a water soluble compound, PVA will be dissolved in the aqueous electrolyte. This would lead to the formation of pores and lead to increased interaction between electrolyte and the active electrode material. But at the same time, dissolution of PVA would also affect the stability of working electrode. Since working electrode was fabricated by filing a Ni gauge with slurry and then uniaxially pressing dried electrode, dissolution of PVA may lead to leaching, especially from the slurry present at the surface of Ni gauge. This may lead to the loss of active material and, in turn, may affect the cycle-ability of the electrode. Here, however, we would like to make it clear that the initial activation process observed during the 1–3 cycles is not due to the dissolution of PVA and resultant pore formation leading to increased electrolyte/electrode interface, because the working electrode was equilibrated by putting it into the electrolyte for 2 h before the commencement of the charge/discharge measurement. A full cell measurement will be free from above drawbacks and we expect that in those conditions $FePO_4$ would show better cyclic-ability as a negative electrode.

Nevertheless, the purpose of this study was to explore the possibility of hydrogen charge/discharge in $FePO_4$ and the experimental results obtained in this work are positive in this aspect. In order to improve the discharge capacity and cyclic stability of $FePO_4$ for electrochemical charge/discharge, various strategies such as modifications of the $FePO_4$ structure, composites with other materials improving charge transfer kinetics, microstructural variations improving the surface area of the active material leading to improvement in the area of the electrode/electrolyte interface (e.g., use of mesoporous material), should be explored [43].

4. Conclusion

Nano-sized amorphous and crystalline $FePO_4$ were synthesized by an alcohol-assisted precipitation method. The electrochemical hydrogen charge/discharge properties of electrodes containing $FePO_4$ as active material were studied in KOH electrolyte for potential application as negative electrodes in rechargeable hydrogen batteries. In galvanostatic discharge/charge mode at 25 °C, the crystalline $FePO_4$ showed the maximum discharge capacity of 109 mA h g^{-1}, while the amorphous $FePO_4$ showed the maximum discharge capacity of 81.4 mA h g^{-1}. XPS data showed that the hydrogen charge/discharge occurs through the redox process associated with the change in oxidation state of Fe in $FePO_4$. The electrochemical kinetic properties, exchange current density, and proton diffusivity were calculated using linear polarization measurement and the potential-step method. The hydrogen diffusion rate was also estimated using the potential-step method. Considering the low cost of $FePO_4$, its environmental friendliness,

and ease of synthesis, $FePO_4$-based materials could be a promising alternative for the negative electrodes in hydrogen batteries.

Acknowledgment

This work was supported by the Priority Research Centers Program through the National Research Foundation of Korea (NRF), and funded by the Ministry of Education, Science, and Technology (2009-0094055).

References

[1] S.G. Chalk, J.F. Miller, Key challenges and recent progress in batteries, fuel cells, and hydrogen storage for clean energy systems, Journal of Power Sources 159 (2006) 73–80.
[2] M. Conte, P.P. Prosini, S. Passerini, Overview of energy/hydrogen storage: state-of-the-art of the technologies and prospects for nanomaterials, Materials Science and Engineering B 108 (2004) 2–8.
[3] Y. Liu, H. Pan, M. Gao, Q. Wang, Advanced hydrogen storage alloys for Ni/MH rechargeable batteries, Journal of Materials Chemistry 21 (2011) 4743–4755.
[4] M.A. Fetcenko, S.R. Ovshinsky, B. Reichman, K. Young, C. Fierro, J. Koch, A. Zallen, W. Mays, T. Ouchi, Recent advances in NiMH battery technology, Journal of Power Sources 165 (2007) 544–551.
[5] X. Li, L. Wang, H. Dong, Y. Song, H. Shang, Electrochemical hydrogen absorbing properties of graphite/AB_5 alloy composite electrode, Journal of Alloys and Compounds 510 (2012) 114–118.
[6] M. Tliha, H. Mathlouthi, C. Khaldi, J. Lamloumi, A. Percheronguegan, Electrochemical properties of the $LaNi_{3.55}Mn_{0.4}Al_{0.3}Co_{0.4}Fe_{0.35}$ hydrogen storage alloy, Journal of Power Sources 160 (2006) 1391–1394.
[7] A.K. Shukla, S. Venugopalan, B. Hariprakash, Nickel-based rechargeable batteries, Journal of Power Sources 100 (2001) 125–148.
[8] I. Saladan, R. Burtovyy, H.W. Becker, V. Ader, C. Woll, Ti–Ni alloys as MH electrodes in Ni–MH accumulators, International Journal of Hydrogen Energy 33 (2008) 7177–7184.
[9] N.H. Goo, J.H. Woo, K.S. Lee, Mechanism of rapid degradation of nanostructured Mg Ni hydrogen storage alloy electrode synthesized by mechanical alloying and the effect of mechanically coating with nickel, Journal of Alloys and Compounds 288 (1999) 286–293.
[10] T. Abe, T. Tachikawa, Y. Hatano, K. Watanabe, Electrochemical behavior of amorphous MgNi as negative electrodes in rechargeable Ni–MH batteries, Journal of Alloys and Compounds 332 (2002) 792–795.
[11] H.H. Lee, K.Y. Lee, J.Y. Lee, Degradation mechanism of Ti–Zr–V–Mn–Ni metal hydride electrodes, Journal of Alloys and Compounds 260 (1997) 201–207.
[12] S.R. Kim, J.Y. Lee, H.H. Park, A study of the activation behaviour of Zr–Cr–Ni–La metal hydride electrodes in alkaline solution, Journal of Alloys and Compounds 205 (1994) 225–229.
[13] M. Anik, Improvement of the electrochemical hydrogen storage performance of Mg_2Ni by the partial replacements of Mg by Al, Ti and Zr, Journal of Alloys and Compounds 486 (2009) 109–114.
[14] H.G. Pan, Y.F. Liu, M.X. Gao, Y.Q. Lei, Q.D. Wang, A study of the structural and electrochemical properties of $La_{0.7}Mg_{0.3}(Ni_{0.85}Co_{0.15})_x$ ($x = 2.5$ 5.0) hydrogen storage alloys, Journal of the Electrochemical Society 150 (2003) A565–A570.
[15] S. Yasuoka, Y. Magari, T. Murata, T. Tanaka, J. Ishida, H. Nakamura, T. Nohma, M. Kihara, Y. Baba, H. Teraoka, Development of high-capacity nickel–metal hydride batteries using superlattice hydrogen-absorbing alloys, Journal of Power Sources 156 (2006) 662–666.
[16] Y.H. Zhang, B.W. Li, H.P. Ren, Z.W. Wu, X.P. Dong, X.L. Wang, Influences of the substitution of Fe for Ni on structures and electrochemical performances of the as-cast and quenched $La_{0.7}Mg_{0.3}Co_{0.45}Ni_{2.55-x}Fe_x$ (x=0–0.4) electrode alloys, Journal of Alloys and Compounds 460 (2008) 414–420.
[17] Y.F. Liu, H.G. Pan, M.X. Gao, R. Li, Q.D. Wang, Intrinsic/extrinsic degradation of Ti–V-based hydrogen storage electrode alloys upon cycling, Journal of Physical Chemistry C 112 (2008) 16682–16690.
[18] H. Miao, M.X. Gao, Y.F. Liu, D. Zhu, H.G. Pan, An improvement on cycling stability of Ti–V–Fe-based hydrogen storage alloys with Co substitution for Ni, Journal of Power Sources 184 (2008) 627–632.
[19] T. Esaka, H. Sakaguchi, S. Kobayashi, Hydrogen storage in proton-conductive perovskite-type oxides and their application to nickel–hydrogen batteries, Solid State Ionics 66 (2004) 351–357.
[20] G. Deng, Y. Chen, M. Tao, C. Wu, X. Shen, H. Yang, M. Liu, Electrochemical properties and hydrogen storage mechanism of perovskite-type oxide $LaFeO_3$ as a negative electrode for Ni/MH batteries, Electrochimica Acta 55 (2010) 1120–1124.
[21] D.K. Lim, K.C. Lee, C.N. Park, S.J. Song, Preparation and hydrogen storage properteis of $BaZr_{0.65}Ce_{0.2}Y_{0.1}Rb_{0.05}O_{3-\delta}$ as the negative electrode of a hydrogen battery, Journal of Ceramic Processing Research 13 (2012) 315–318.
[22] R. Tahir, K. Banert, S. Sebti, Natural and synthetic phosphates: new and clean heterogeneous catalysts for the synthesis of 5-arylhydantoins, Applied Catalysis A: General 298 (2006) 261–264.
[23] M. Edwards, L. Hidmi, D. Gladwell, Phosphate inhibition of soluble copper corrosion by-product release, Corrosion Science 44 (2002) 1057–1071.
[24] A.K. Padhi, K.S. Nanjundaswamy, J.B. Goodenough, Phospho-olivines as positive-electrode materials for rechargeable lithium batteries, Journal of the Electrochemical Society 144 (1997) 1188–1194.
[25] T. Shiratsuchi, S. Okada, J. Yamaki, T. Nishida, $FePO_4$ cathode properties for Li and Na secondary cells, Journal of Power Sources 159 (2006) 268–271.
[26] Z.C. Shi, A. Attia, W.L. Ye, Q. Wang, Y.X. Li, Y. Yang, Synthesis, characterization and electrochemical performance of mesoporous $FePO_4$ as cathode material for rechargeable lithium batteries, Electrochimica Acta 53 (2008) 2665–2673.
[27] H.C. Liu, W.H. Ho, C.F. Li, S.K. Yen, Electrochemical synthesis of $FePO_{(4)}$ for anodes in rechargeable lithium batteries, Journal of the Electrochemical Society 155 (2008) E178–E182.
[28] C. Masquelier, P. Reale, C. Wurm, M. Morcrette, L. Dupont, D. Larcher, Hydrated iron phosphates $FePO_4 \cdot n\,H_2O$ and $Fe_4(P_2O_7)_3 \cdot nH_2O$ as 3 V positive electrodes in rechargeable lithium batteries, Journal of the Electrochemical Society 149 (2002) A1037–A1044.
[29] Y. Song, S. Yang, P.Y. Zavalij, M.S. Whittigham, Temperature-dependent properties of $FePO_4$ cathode materials, Materials Research Bulletin 37 (2002) 1249–1267.
[30] P.P. Prosini, M. Lisi, S. Scaccia, M. Carewska, F. Cardellini, M. Pasquali, Synthesis and characterization of amorphous hydrated $FePO_4$ and its electrode performance in lithium batteries, Journal of the Electrochemical Society 149 (2002) A297–A301.
[31] K. Zaghib, C.M. Julien, Structure and electrochemistry of $FePO_4 \cdot 2H_2O$ hydrate, Journal of Power Sources 142 (2005) 279–284.
[32] S. Okada, T. Yamamoto, Y. Okazaki, J.I. Yamaki, M. Tokunaga, T. Nishida, Cathode properties of amorphous and crystalline $FePO_4$, Journal of Power Sources 146 (2005) 570–574.
[33] X. Wang, X.H. Yang, H.G. Zheng, H.Y. Jin, Z. Zhang, Synthesis and electrochemical performance of amorphous hydrated iron phosphate nanoparticles, Journal of Crystal Growth 274 (2005) 214–217.
[34] J. Kang, V. Mathew, J. Gim, S. Kim, B.J. Paul, J. Song, A.K. Rai, J. Han, D. Ahn, J.Y. Lee, J. Kim, An amorphous/crystalline reconstitutive reaction in nanostructured phosphate electrodes for Li/Na/K batteries. Energy and Environmental Science, submitted for publication.

[35] G. Deng, Y. Chen, M. Tao, C. Wu, X. Shen, H. Yang, M. Liu, Electrochemical properties and hydrogen storage mechanism of perovskite-type oxide $LaFeO_3$ as a negative electrode for Ni/MH batteries, Electrochimica Acta 55 (2010) 1120–1124.

[36] B. Liao, Y.Q. Lei, L.X. Chen, Effect of the La/Mg ratio on the structure and electrochemical properties of $La_xMg_{3-x}Ni_9$ (x= 1.6–2.2) hydrogen storage electrode alloys for nickel–metal hydride batteries, Journal of Power Sources 129 (2004) 358–367.

[37] M.Y. Song, D. Ahn, I.H. Kwon, S.H. Chough, Development of AB_2-type Zr–Ti–Mn–V–Ni–M hydride electrode for Ni–MH secondary battery, Journal of the Electrochemical Society 148 (2001) A1041–1044.

[38] T. Kohno, H. Yoshida, F. Kawashima, T. Inaba, I. Sakai, M. Yamamoto, M. Kanda, Hydrogen storage properties of new ternary system alloys: La_2MgNi_9, $La_5Mg_2Ni_{23}$, La_3MgNi_{14}, Journal of Alloys and Compounds 311 (2000) L5–L7.

[39] P.H.L. Notten, R.E.F. Einerhand, J.C.L. Daams, On the nature of the electrochemical cycling stability of non-stoichiometric $LaNi_5$-based hydride-forming compounds Part I. Crystallography and electrochemistry, Journal of Alloys and Compounds 210 (1994) 221–232.

[40] M. Raju, M.V. Anantha, L. Vijayaraghavan, Influence of temperature on the electrochemical characteristics of $MmNi_{3.03}Si_{0.85}Co_{0.60}Mn_{0.31}Al_{0.08}$ hydrogen storage alloys, Journal of Power Sources 180 (2008) 830–835.

[41] M. Minakshi, D.R.G. Mitchell, The influence of bismuth oxide doping on the rechargeability of aqueous cells using MnO_2 cathode and LiOH electrolyte, Electrochimica Acta 53 (2008) 6323–6327.

[42] M. Minakshi, D.R.G. Mitchell, P. Singh, TEM investigation of MnO_2 cathode containing TiS_2 and its influence in aqueous lithium secondary batteries, Electrochimica Acta 52 (2007) 3294–3298.

[43] C. Liu, F. Li, L.P. Ma, H.M. Cheng, Advanced materials for energy storage, Advanced Materials 22 (2010) E28–E62.